

Computation of the Flow in a H.P. Compressor Drive Cone Cavity

Kok M THAM^{1,*}, Christopher A LONG², Alan B TURNER³ and Jeffrey A DIXON⁴

^{1,2,3} Thermo-Fluid Mechanics Research Centre
University of Sussex

Falmer, Brighton, East Sussex BN1 9QT, UNITED KINGDOM

Phone: +44 (0)1273 678945, Fax: +44 (0)1273 678486, E-mail: C.A.Long@sussex.ac.uk

⁴Rolls-Royce plc, P. O. Box 31, Derby DE24 8BJ, UNITED KINGDOM

ABSTRACT

In some modern aero-engines, the H.P. drive cone cavity is used to deliver cooling air bled from the last stage of the H.P. compressor to the turbine blades, or simply to ventilate the cavity to prevent excessive heating. Engine designers are concerned about the temperature rise of the cooling air due to viscous dissipation and heat transfer. Using an engine-representative geometry, and matching non-dimensional parameters typical of modern turbofans, laser Doppler anemometry measurements were complemented by steady, axisymmetric, CFD computations using the commercial code FLUENT. The experimental results reinforce previous findings in the upstream cavity, and new velocity measurements in the downstream cavity are also presented.

In general, CFD tends to underpredict the core swirl ratio in the drive cone cavity, with agreement improving with decreasing $|\lambda_{\text{turb}}|$, but the Rankine vortex profile was well predicted. For the downstream cavity, measurements and computations show a radial distribution of tangential velocity of a Rankine vortex, with a stronger free vortex component than the upstream cavity. CFD flow patterns and velocity distributions suggest a departure from a rotationally- to a throughflow-dominated flow regime as throughflow rates are increased; a demarcation parameter of $|\lambda_{\text{turb}}| = 0.1$ is suggested.

NOMENCLATURE

a, b	inner and outer radii of disc, cone, or cylinder, respectively
A, B	constants in Eq. (1)
$c = \frac{V_{\phi,b}}{\Omega b}$	inlet swirl fraction into cone cavity
$C_w = \frac{\dot{m}}{\mu b}$	non-dimensional mass flow rate
d	hydraulic diameter
I	turbulence intensity
\dot{m}	mass flow rate
r	radial coordinate
$Re_d = \frac{\rho U d}{\mu}$	Reynolds number based on hydraulic diameter
$Re_\phi = \frac{\rho \Omega b^2}{\mu \sin \theta}$	rotational Reynolds number
U	bulk axial velocity in compressor stage

V_r	radial velocity
V_z	axial velocity
V_ϕ	tangential velocity
w	maximum axial width of cone cavity
$x = r / b$	non-dimensional radius
$y = z / w$	non-dimensional axial distance
z	axial coordinate
$\beta = \frac{V_{\phi,\text{core}}}{\Omega r}$	core swirl ratio
$\lambda_{\text{turb}} = \frac{C_w}{Re_\phi^{0.8}}$	turbulent flow parameter
μ	dynamic viscosity
θ	cone half angle ($= 27^\circ$)
ρ	density
Ω	angular speed of rotor

Superscript

* no throughflow value

Subscripts

b disc or cone outer radius value
core fluid core value

1. INTRODUCTION

A feature found in the internal air systems of some gas turbine aero-engines is the H.P. drive cone cavity, which is the space formed between a conical shaft or a drive cone (for driving the H.P. compressor from the H.P. turbine), and the combustor inner casing. This conical cavity is located at the heart of the engine. The drive cone is also one of the hottest parts in the engine, where temperatures of up to 900 K at 10,000 rpm are not uncommon. Air bled from the last stage of the H.P. compressor for turbine blade cooling is routed via the cone cavity, in some engine designs. The air extracted from this annular slot downstream of the compressor blade is parasitic to the main cycle (especially so at the last stage of H.P. compression), as it would otherwise participate in the combustion process and drive the H.P. turbine. At high rotational speeds, windage heating (viscous dissipation) is also important, making the cavity ventilation air and/or turbine blade cooling air susceptible to temperature rises from windage and heat transfer, resulting in lower allowable compressor delivery and turbine entry temperatures, or higher bleed flows.

The internal air systems designer's aim is therefore to extract the least amount of air, thereby optimising the thermodynamic efficiency, whilst ensuring adequate cooling and sealing. From

* Now at Lotus Engineering Malaysia Sdn. Bhd., Malaysia

Copyright © 2003 by GTSJ

Manuscript Received on April 17, 2003

stress and life considerations, for materials required to operate close to their temperature limits, a 10 K reduction in surface temperature can double its life. A good knowledge of the drive cone temperature distribution can potentially lead to the selection of a cheaper or lighter material, or a longer declared life, offsetting the potential costs of depreciation. A common requirement is a good knowledge of the flow and heat transfer in the cone cavity. A natural analysis option would be computational fluid dynamics (CFD). Recently, the frontiers of complexity and size of the CFD models have been progressively pushed, heading towards an attractive goal in industry — to be fully predictive using CFD. However, understanding must come before prediction. Using the same experimental apparatus, this paper builds on the results and understanding from Long et al. (2003); further flow measurements in the cone cavity are presented, complemented by steady, axisymmetric CFD calculations. Experimental data was obtained at non-dimensional conditions resembling modern aero-engines, using a full-scale engine-representative geometry.

There is little published research for conical cavities. In comparison, the free-cone system has received more attention in the past (see, for example, Wu, 1958 and Chew, 1985), with its roots firmly in free-disc analyses, utilising the momentum-integral approach previously applied with much success. Experiments by Yamada and Ito (1979) on a cone rotor-stator system with radial outflow showed the presence of Taylor-type vortices, which can be suppressed by either increasing the rotor-stator gap, the rotational Reynolds number, or the throughflow rate. Streamlines from finite-difference computations by May et al. (1994), for the same geometry, showed a flow structure similar to classical rotor-stator systems, i.e. radial outflow and inflow respectively in the boundary-layers on the rotor and stator surfaces, with a core rotating at less than rotor speed. From Long et al. (2003), with superposed inflow, LDA measurements in the upstream cavity indicate a combined free and forced vortex: the Rankine vortex; without throughflow, forced vortex motion occurs. From Gan et al. (1996), the Rankine vortex velocity distribution is given by

$$\beta = \frac{V_{\phi,core}}{\Omega r} = \frac{A}{x^2} + B \quad (1)$$

where A and B are invariant with radius. This Rankine vortex flow is also found between a pair of co-rotating discs with a rotating inner cylinder, enclosed by a stationary cylindrical outer casing; see Gan et al. (1996), Mirzaee et al. (1998), and Jaafar et al. (2000), where air enters the system through holes or nozzles on the casing, and leaves via the annular clearance between the casing and the rotor. It was shown that the flow structure depended strongly on the turbulent flow parameter, λ_{turb} , defined by

$$\lambda_{turb} = \frac{C_w}{Re_{\phi}^{0.8}} \quad (2)$$

For a cone of outer radius, b, cone half angle, θ , rotating at angular velocity, Ω , in a fluid of dynamic viscosity, μ , and density, ρ , the rotational Reynolds number is defined as

$$Re_{\phi} = \frac{\rho \Omega b^2}{\mu \sin \theta} \quad (3)$$

For radial inflow systems, it is known that the inlet swirl fraction, c, has a strong influence on the cavity flow structure, and is defined by

$$c = \frac{V_{\phi,b}}{\Omega b} \quad (4)$$

where $V_{\phi,b}$ is the tangential velocity at the rim of the disc or cone.

2. EXPERIMENTAL APPARATUS

A general assembly of the test rig is shown in Fig. 1. The rig was constructed using real engine rotor parts, with a mild steel casing encompassing the rotor and bearing assemblies from the H.P. system of a development variant of the Rolls-Royce RB211 engine. This ensured a truly engine-representative geometry. Referring to Fig. 1, the rotor consists of the H.P. compressor stack (six stages), the H.P. drive cone, the mini-disc, and the H.P. turbine disc. The inner radius, a, of the drive cone is 189.50 mm and the outer radius, b, is 328.57 mm. Defining the radius ratio, x, as $x = r / b$, where r is the radial coordinate, the radius ratio at the drive cone inner radius is 0.58. The outer radius of the central shaft is 85 mm and the inner radius of the sixth stage compressor disc is 91.95 mm. For simplicity, the simulated intermediate pressure (I.P.) shaft rotated at the same speed as the drive cone. This differs from normal engine practice where the I.P. system rotates at a lower speed (7,000 rpm) than the H.P. system (10,000 rpm).

From Fig. 1, it is clear that the cone half angle, θ , changes continuously from inner to outer radii. For simplicity in the calculation of the rotational Reynolds number, an area-weighted average of $\theta = 28^\circ$ was obtained; but, to ensure consistency with Rolls-Royce, $\theta = 27^\circ$ was used.

The rig has a design speed of 7,300 rpm, with the sixth stage H.P. compressor blades retained to maintain engine representative conditions at the inlet of the drive cone cavity. However, the height of the 80 original H.P. compressor blades was reduced, as the annulus area was scaled down, in accordance with the rig mainstream annulus mass flow rates (up to 7 kg/s at design conditions). After the H.P. compressor stage, some of the mainstream flow will be bled into the cone cavity. The remainder of the mainstream flow was used to drive the rig, by the turbine stage with a set of 92 reduced height turbine blades, as the power requirements for the rig was much lower relative to the engine. The cone cavity flow leaves the cavity through an annular wall with 30 radial holes of 12 mm diameter, after which the flow was collected in an annular collection chamber, and leaves the chamber via a 52 mm inside diameter cast iron pipe.

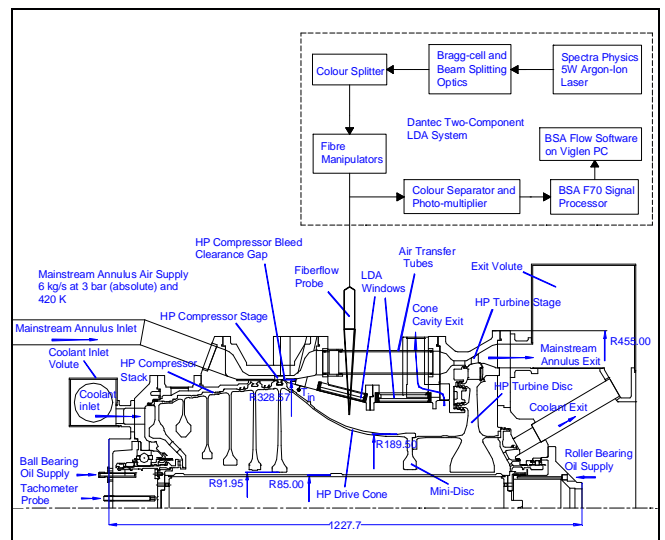


Fig. 1 General assembly of the H.P. Compressor Drive Cone Rig

For the mainstream air supply, the rig had access to two independent compressed air supplies, one being a Rolls-Royce Dart RD7 compressor (10 kg/s at 3 bar (absolute) and 473 K) driven by a Rolls-Royce Dart RD12 engine. For a detailed description of this novel gas turbine-driven centrifugal compressor, the reader is

referred to Turner et al. (2000). Alternatively, the mainstream flow was provided by two Keith-Blackman compressors, each capable of supplying mass flow rates of up to 1.1 kg/s at 1.6 bar (absolute) and 378 K. The axial throughflow of cooling air through the bores of the compressor discs, and thereafter to the drive cone and turbine inner cavities, was provided by an Atlas-Copco ZT-250 two stage rotary screw air compressor (0.8 kg/s at 8 bar (absolute) and 298 K), driven by a 250 kW totally enclosed squirrel cage induction motor. The mainstream mass flow rates from either of these sources were measured with venturi meters; the axial throughflow of coolant air and the cone cavity mass flow rate were measured with orifice plates. All the flow meters conform to BS1042 (British Standards Institute, 1992).

Velocity measurements in the cone cavity were undertaken with a two-component Dantec FiberFlow laser Doppler anemometry (LDA) system operating in backscatter mode, which consisted of: a 5 W water-cooled Spectra-Physics Argon-Ion laser; transmitting optics that included a Bragg-cell, a colour splitter, and a 27 mm diameter two-component FiberFlow probe, with focal lengths of 100 mm and 250 mm, respectively; receiving optics which comprised a focusing lens, a colour separator (488 nm and 514.5 nm interference filters), and a photo-multiplier; a BSA F70 signal processor (160 MHz Doppler frequency with 120 MHz bandwidth); BSA flow software; and a Viglen Contender P3-800 PC. The measurement planes for the LDA tests are shown in Fig. 2, where in the upstream cavity the radial variation of tangential velocity is measured at $y = z / w = 0.36$, where z is the axial coordinate, and w is the maximum width of the cavity from the cone outer radius to the turbine disc upstream surface (478.15 mm); for the downstream cavity, the axial and tangential velocities are measured at $y = 0.61$ and 0.65 . Optical access into the cone cavity was achieved via BK7 fused silica glass windows. The measurement volume dimensions for the blue and green colour beams are given in Table 1:

Table 1 Measurement volume dimensions for blue (488 nm) and green (514.5 nm) beams

Beam Wavelength (nm)	Focal Length (mm)	Diameter (mm)	Length (mm)	Fringe Spacing (μm)
488	100	0.046	0.61	3.26
488	250	0.115	3.84	8.14
514.5	100	0.049	0.65	3.44
514.5	250	0.121	4.04	8.58

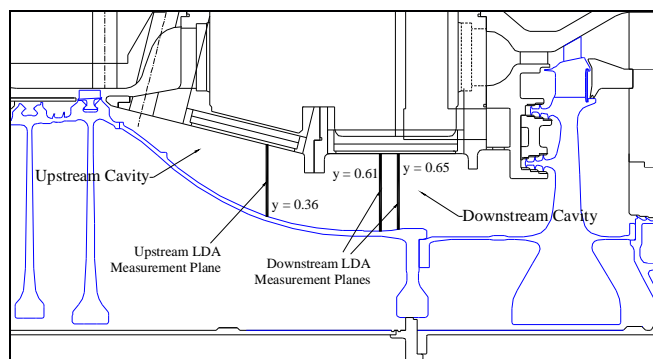


Fig. 2 LDA measurement planes

3. CFD: THE 2D CFD MODEL

The CFD calculations were performed using an axisymmetric, steady-state model, using the commercial finite volume code FLUENT. This involved some simplifications to the

three-dimensional (3D) features in and around the cone cavity. The compressor blades were not modelled, and the inlet to the CFD model was located at the exit of the H.P. compressor. At the cone cavity exit, the equispaced circumferential array of 30 holes of 12 mm diameter was replaced with an axisymmetric slot of equivalent area, and the midpoint of the slot was aligned with the axis of the holes. The turbine inner labyrinth seal leakage flow was also assumed to be negligible. For an economical mesh size, the meshing strategy encompassed the subsequent use of wall functions in the solver. Thus the height of the wall-adjacent cells was chosen to ensure that the non-dimensional near wall spacing, y^+ , lie within the range of applicability of wall functions ($30 < y^+ < 100$). The values of y^+ are solution-dependent; hence, three unstructured meshes were produced in GAMBIT (1998), each with approximately 60,000 cells, catering to the respective flow conditions. Mesh-dependency was checked with a 220,000-cell model, whilst retaining the near-wall grid spacing, thus ensuring any changes in the solution are due to errors in the region outside the wall-adjacent cells. In all the meshes only quadrilateral elements were utilised; this enabled the use of the PRESTO! (PRESSure STaggering Option) pressure interpolation scheme in the FLUENT solver, recommended for high-speed rotating flows. Fig. 3 shows the computational mesh: there are one inlet and two exits in the solution domain. The mainstream inlet and exits are marked "Inlet 1" and "Exit 1", respectively; "Exit 2" indicates the cone cavity exit. It was essential to have a fully-developed flow at the exit boundaries, to avoid errors due to flow reversal. From the subsequent solutions, no reverse flow was evident at the annulus and cone exits ("Exit 1" and "Exit 2", respectively); hence, the locations of the exit boundaries were deemed satisfactory.

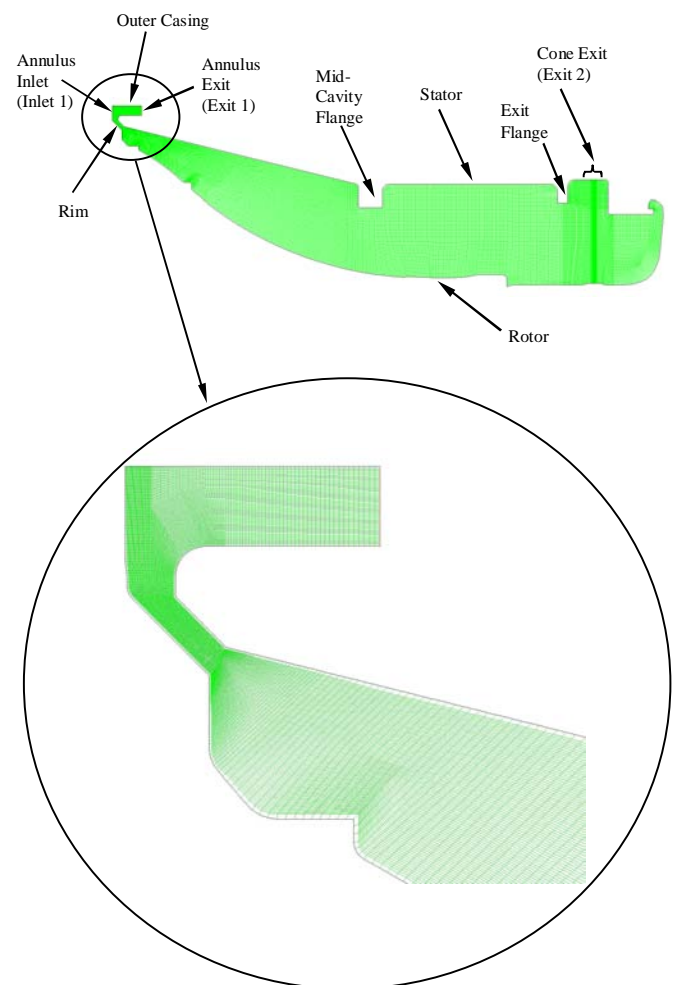


Fig. 3 The 2D CFD model

The annulus inlet was represented by a mass flow inlet boundary condition: the measured total temperature upstream of the H.P. compressor blades, the measured mass flow rates from the Dart or Blackman compressors, and the flow direction were specified. Radial flow was ignored; the axial flow direction vector was calculated from continuity; for simplicity, the tangential flow direction was found from the compressor velocity triangles, ignoring tip clearance effects. This approach was considered adequate, as a full 3D analysis modelling tip-leakage flow had been undertaken by Long et al. (2003), and the predictions ignoring the compressor blade clearance were still satisfactory. The turbulence quantities specified at the inlet were the intensity and hydraulic diameter, being 4% (typically) and 0.02 m, respectively, from the empirical correlation for pipe flows (FLUENT, 1998)

$$I \cong 0.16(\text{Re}_d)^{-1/8} \quad (5)$$

where Re_d is a flow Reynolds number based on the hydraulic diameter. The suitability of the location of the inlet was checked by using an alternative inlet boundary condition (a total pressure inlet), where keeping the boundary conditions identical, and by adjusting the total pressure at the inlet to obtain the desired mass flow rate, the tangential velocities in the upstream LDA plane were found to differ by less than 1.5%.

For all cases, pressure outlet boundary conditions were used at the annulus exit (“Exit 1”) and cone exit (“Exit 2”); the static pressure measured directly at the exit of the compressor was specified for the former, and the static pressure at the latter was adjusted until the desired cone throughflow rate was obtained. The calculations were performed with the commercial finite volume solver, FLUENT. The Reynolds-averaging approach for the Navier-Stokes equations was adopted, where the equations were closed by the use of the high-turbulence-Reynolds-number $k-\epsilon$ model by Launder and Spalding (1972).

The turbulence model mentioned above is only valid for fully turbulent flows, and close to the walls, where the molecular viscosity is important (attenuating the turbulent fluctuations), FLUENT offers two options for the near-wall modelling: the substitution of the $k-\epsilon$ model with logarithmic wall functions; and a two-layer zonal model, where the flow is resolved all the way to the wall. The two-layer approach was found to agree with the wall functions treatment, therefore only wall functions calculations are presented here. As the Navier-Stokes and energy equations are decoupled, the governing equations are solved sequentially and implicitly. The SIMPLE (Semi-Implicit Method for Pressure-Linked Equations) algorithm of Patankar and Spalding (1972) was used for the pressure-velocity coupling. A second order upwind (values derived from upstream cell) discretisation scheme was used for the continuity equation, momentum equations, energy equation, and the transport equations for the turbulence kinetic energy and its dissipation rate. Viscous dissipation (important for high-Reynolds-number flows) was included in the solutions, and the density was calculated from the ideal gas law. The dynamic viscosity was evaluated using Sutherland’s law.

A solution is judged to have converged, if: residuals for each variable level off over the number of iterations; a mass and heat balance is satisfied across all boundaries of the solution domain; and, in this case for rotating flows, conservation of angular momentum, including the monitoring of the rotor frictional moment. The mass flow rate in FLUENT was always found to agree within the measured value to 3%, which is the estimated value of uncertainty in the measurement.

The net mass flow across all the inlet and exits were of the order of 10^{-7} kg/s; normalising the net mass flow by the cavity

throughflow rate, the mass flow error is less than 0.05%. The net heat transfer across all boundaries usually balanced to within 1% of the inlet enthalpy; and the net angular momentum flux through inlet and exits differed from the net torque in the system by 3% to 17%.

4. RESULTS FROM LDA MEASUREMENTS AND COMPARISON WITH CFD

4.1 Upstream Cavity

The measured and predicted radial distribution of $V_\phi / \Omega r$ is shown in Fig. 4 for the inlet swirl fraction, $c = 0.3$; the plane at $y = 0.36$ was used (see Fig. 2). As mentioned earlier, c was obtained using the compressor velocity triangles, ignoring tip leakage. Note that for radial inflow, C_w is defined as negative. For no throughflow, the predicted core swirl ratio agreed well with experiments, and also with the theoretical value of 0.426 by Owen (1988), for turbulent flow between a rotating and a stationary disc. There is consistent underprediction of the tangential velocities, with the discrepancy increasing with $|C_w|$, i.e. with $|\lambda_{\text{turb}}|$. It is unlikely that this is due to the omission of compressor blade tip clearance effects in the definition of the inlet velocity vector; inclusion will only reduce the effective inlet swirl into the cavity. Nevertheless, the agreement is still considered fair; the qualitative prediction being satisfactory. Measurements of the axial velocities were not conducted for these conditions.

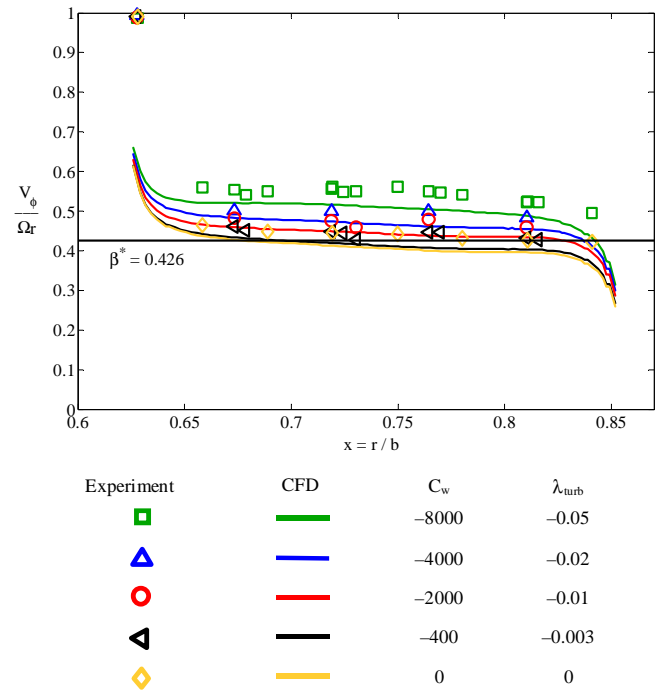


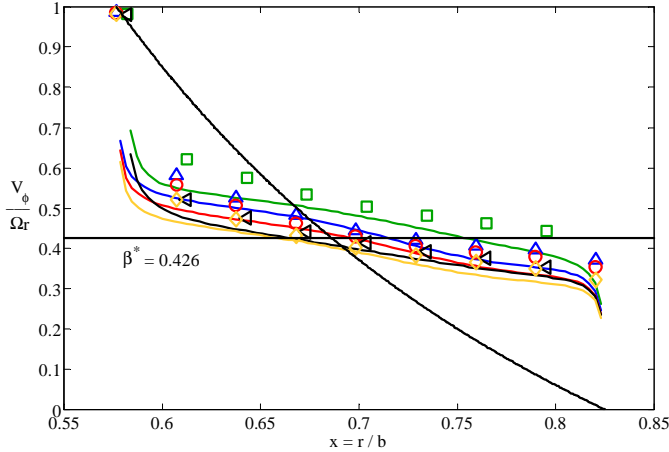
Fig. 4 Measured (LDA) and computed effect of $|C_w|$ on $V_\phi / \Omega r$, for the upstream cavity, for $\text{Re}_\phi = 3 \times 10^6$, $c = 0.3$

4.2 Downstream Cavity

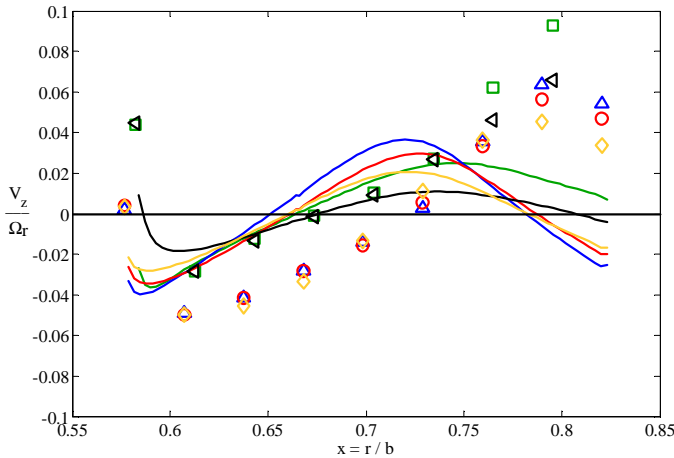
For the downstream cavity, referring to the planes $y = 0.61$ and 0.65 , the radial distribution of $V_\phi / \Omega r$ is shown in Fig. 5 (a). In general, there is an underprediction of the tangential velocities, becoming more apparent with increasing inflow. But the agreement is still considered satisfactory, with the Rankine vortex profile being well predicted. Also, CFD again agreed well with theory ($\beta^* = 0.426$), for no throughflow. Also shown is the analytical solution by Taylor (1923) for steady, axisymmetric flow (rotation only, $V_r = V_z = 0$) between two concentric cylinders; for an inner cylinder (of radius a) rotating at rotational speed, Ω , with a stationary outer cylinder (of radius b), the solution is given by

$$\frac{V_\phi}{\Omega r} = \frac{(ab)^2}{(b^2 - a^2)r^2} + \frac{a^2}{a^2 - b^2} \quad (6)$$

Interestingly, the solution (also termed rotating Couette flow) is a particular form of the Rankine vortex (Eq. (1)). The cases for small inflow ($|C_w| \leq 2000$) best replicate the conditions assumed in the theoretical solution of Taylor (1923), and the measured values of $V_\phi / \Omega r$ lie between the theoretical forced vortex line for no throughflow ($\beta^* = 0.426$) and rotating Couette flow (merged boundary layers). As expected from the conservation of angular momentum, the swirl ratio of the core increased with $|C_w|$. The measured values of $V_\phi / \Omega r$ for $0.68 \leq x \leq 0.82$ and $|C_w| \leq 4000$ being less than 0.426 can also be explained by the influence of rotating Couette flow, in the downstream cavity.



(a) Tangential Velocity



(b) Axial Velocity

Experiment	CFD	C_w	λ_{turb}
\square	---	-8000	-0.05
\triangle	---	-4000	-0.02
\circ	---	-2000	-0.01
\blacktriangleleft	---	-800	-0.005
\diamond	---	0	0

Fig. 5 Measured and computed velocities for the downstream cavity, for $Re_\phi = 3 \times 10^6$, $c = 0.3$

Correspondingly, the computed radial distribution of $V_z / \Omega r$ is shown in Fig. 5 (b). The measured data for all $|C_w|$ indicates that a

central core ceases to exist, with merged boundary layers, and this is consistent with the tangential velocity distribution shown in Fig. 5 (a). The agreement between experiment and CFD is poor for this case, but it must be remembered that the LDA probe was susceptible to alignment errors, which propagate well into the measured V_z , for a strongly rotating flow. A more likely factor is the well-documented shortcomings of the standard wall functions for flows involving separation; the flow is expected to separate downstream of the mid-cavity flange (see Fig. 3), and the calculation of V_z will obviously be sensitive to the separation and the subsequent reattachment point. Nevertheless, the good overall agreement for the tangential and axial velocities gives confidence in the predicted flow structure. Hence calculations were extended to $|\lambda_{turb}| = 0.8$, to investigate numerically the flow structure at high inflow rates. The results are shown in the next section.

5. FLOW STRUCTURE FOR LARGE VALUES OF $|\lambda_{turb}|$ FROM CFD

The relatively good agreement between the measured and computed velocities gave confidence in the use of CFD to predict the flow structure in the cavity. The axisymmetric models used in the previous computations were also used for these simulations for large values of $|\lambda_{turb}|$. Only $|C_w|$ was varied to obtain the range of $|\lambda_{turb}|$, and not Re_ϕ , because the y^* values would still lie in the permissible range for wall functions. It is now of interest to examine the computed streamlines for high throughflow rates for any change of flow regime, from being rotationally-dominated (as shown in Section 4).

The computed streamlines are grouped according to common values of $|\lambda_{turb}| = 0, 0.02, 0.05, 0.1, 0.2, 0.4$, and 0.8 , and are shown in Fig. 6. The computations were undertaken for $Re_\phi = 2 \times 10^6, 3 \times 10^6, 6 \times 10^6$, and 2×10^7 , with the value of $|C_w|$ adjusted to obtain the desired $|\lambda_{turb}|$, with the inlet swirl, c , between 0.3 and 0.5. From the streamlines for $0 \leq |\lambda_{turb}| \leq 0.8$, it can be concluded that: the flow structure depends principally on $|\lambda_{turb}|$, as for disc rotor-stator systems; which is expected, considering that the velocity measurements have previously showed many similarities with classical rotor-stator systems. Also, the streamlines for $|\lambda_{turb}| = 0.1$, compared with, for example, those for $|\lambda_{turb}| = 0.05$, do show the onset of the prevalence of the throughflow over rotation: for $|\lambda_{turb}| = 0.1$ (see Fig. 6), there is a more noticeable radial penetration of the inflow onto the drive cone surface midway between the cone inner and outer radii, separating the upstream cavity core region and the recirculation in the downstream cavity; the core region in the upstream cavity was slightly suppressed compared with $|\lambda_{turb}| = 0.05$; and the recirculation region adjacent to the H.P. turbine disc in the downstream cavity also grew smaller. These features become more distinct for increasing values of $|\lambda_{turb}|$, until it there is axial flow on the drive cone surface towards the cone exit. These suggest the demarcation point of $|\lambda_{turb}| \approx 0.1$ for transition to a throughflow-dominated regime, from one where rotation prevailed.

The presence of a gap recirculation zone (GRZ) in the rim region is also consistent with earlier results in Long et al. (2003), and is shown in Fig. 7 (a), for relatively small throughflow rates ($Re_\phi = 3 \times 10^6$, $|C_w| = 8000$, $|\lambda_{turb}| = 0.5$, $c = 0.3$). The GRZ was first found in the computations of Ko and Rhode (1992), and have implications on blade platform temperatures, by transporting heat from the mainstream. This clockwise GRZ is due to: the mainstream flow “pushing” the cavity flow; and centrifugal pumping of the drive cone. With increasing inflow, there is a gradual suppression of the gap recirculation zone, and at sufficiently high flow rates (e.g. at $Re_\phi = 2 \times 10^6$, $|C_w| = 81000$, $|\lambda_{turb}| = 0.8$, $c = 0.3$), the GRZ is completely suppressed (see Fig. 7 (b)).

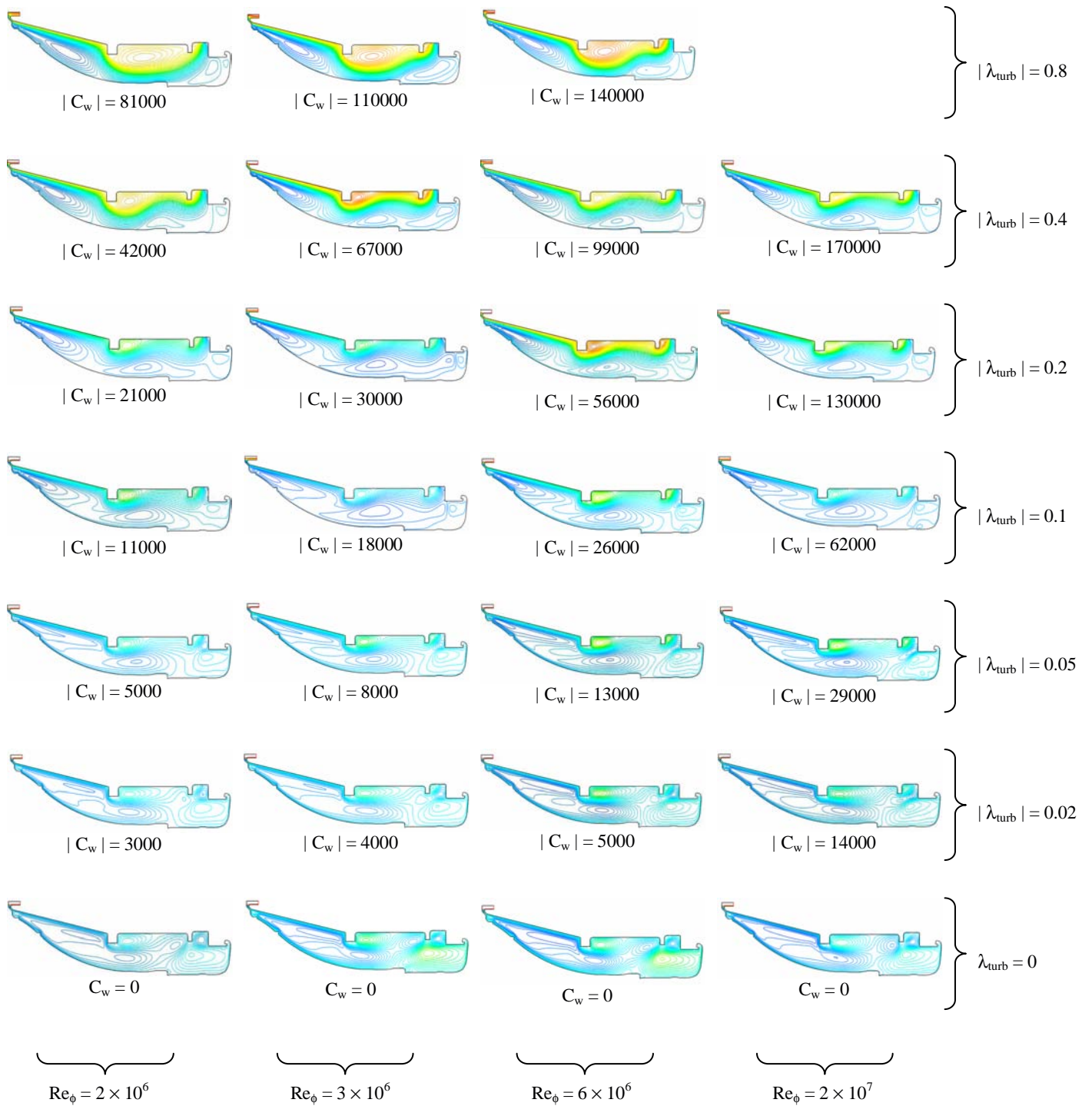


Fig. 6 Computed streamlines from CFD, for $0.3 \leq c \leq 0.5$



(a) Small inflow

(b) Large inflow

Fig. 7 Streamlines of rim region flow from CFD

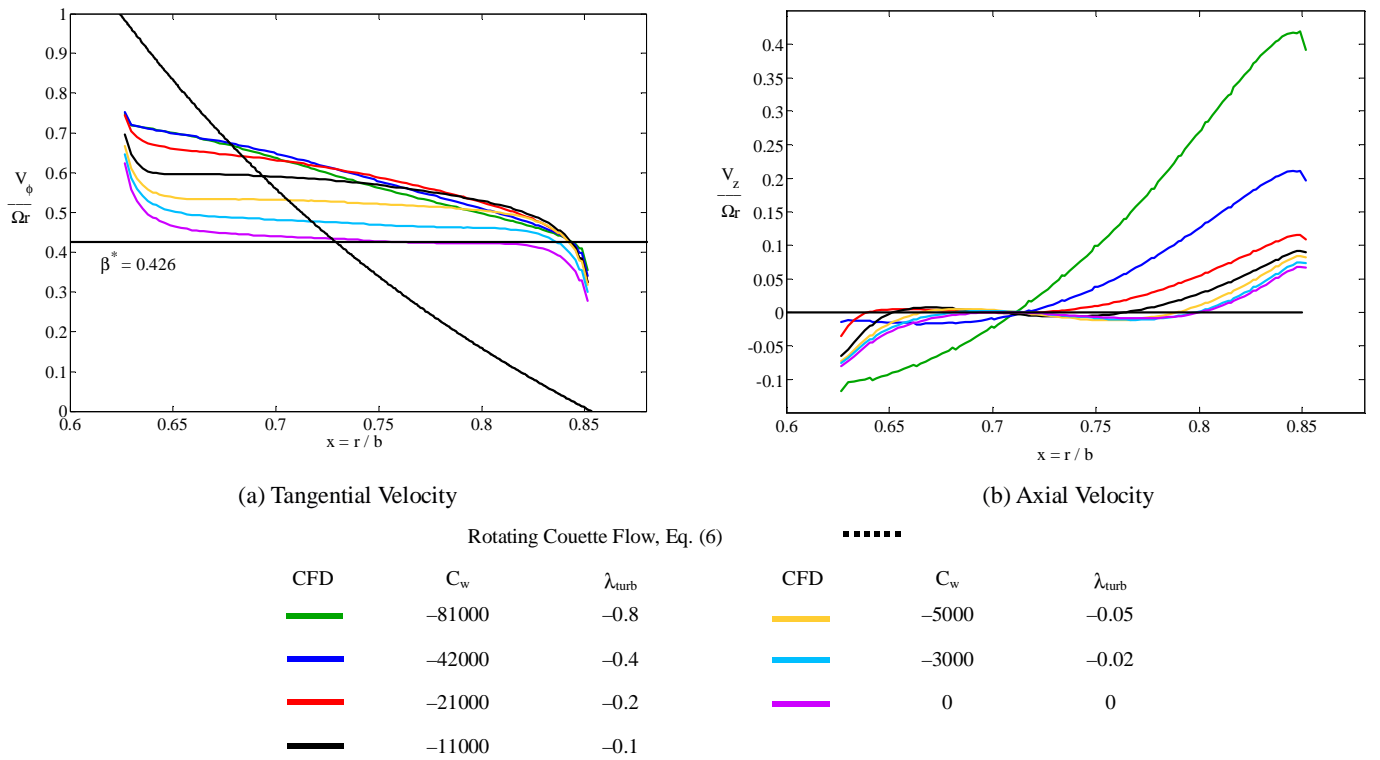


Fig. 8 Predicted velocity profiles for $Re_\phi = 2 \times 10^6$, $c = 0.3$, for the upstream cavity plane at $y = z / w = 0.36$

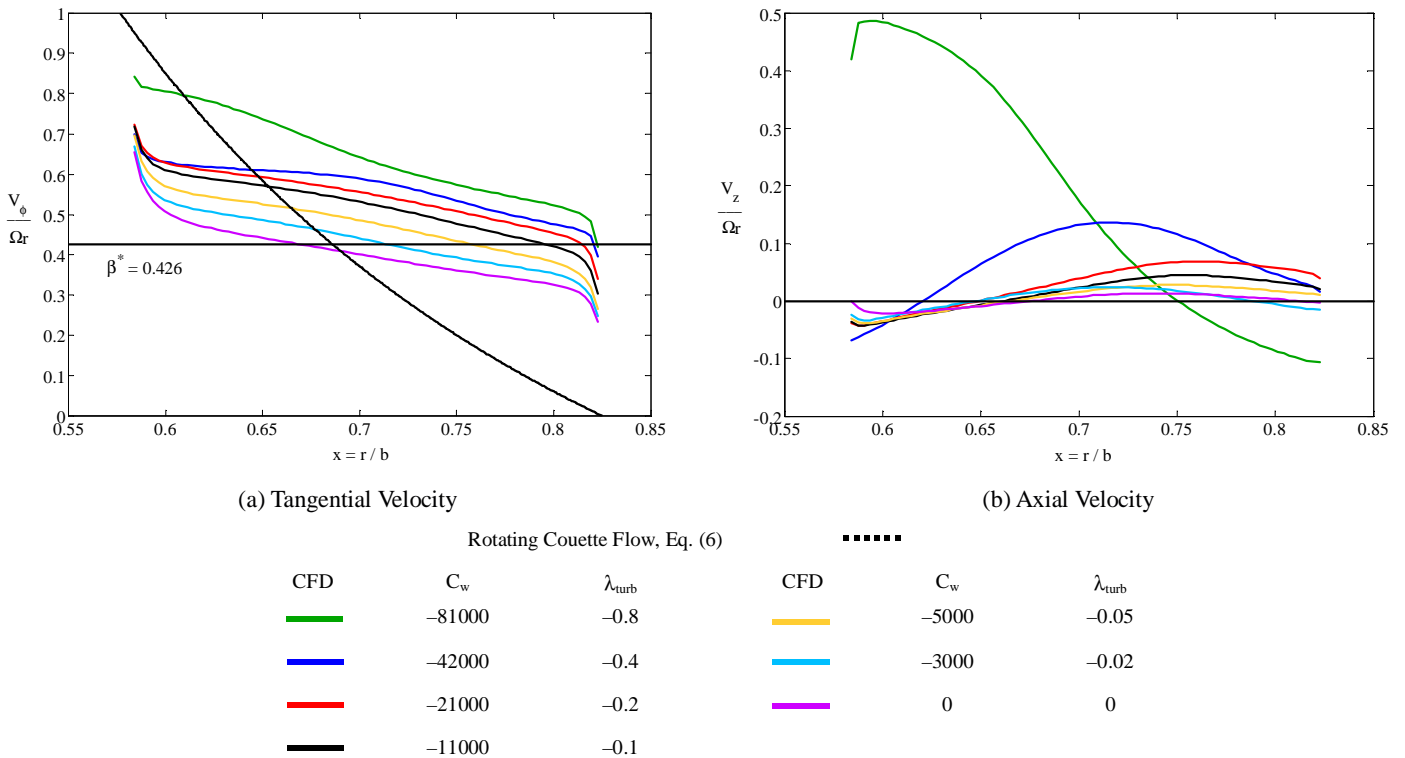


Fig. 9 Predicted velocity profiles for $Re_\phi = 2 \times 10^6$, $c = 0.3$, for the downstream cavity plane at $y = z / w = 0.65$

The predicted tangential and axial velocity profiles are shown at the measurement planes at $y = 0.36$ and 0.65 , for the upstream and downstream cavities, respectively. All the results were independent of Re_ϕ , hence the velocity profiles are shown for $Re_\phi = 2 \times 10^6$ only. The predicted radial distribution of $V_\phi / \Omega r$ for the upstream cavity at the plane $y = 0.36$ is shown in Fig. 8 (a). Notably, for $x \geq 0.73$ and

$|C_w| \geq 0$, the core swirl ratio stays at or above the theoretical value of 0.426; and with increasing inflow, the radial profile of tangential velocity approaches rotating Couette flow, qualitatively (free vortex component gaining strength over forced vortex). It is also clear that for $|C_w|$ up to 11000, there is a marked increase in the overall swirl level with increasing $|C_w|$. Interestingly, a plateau is

reached for the overall level of swirl beyond $|C_w| = 11000$, which is $|\lambda_{\text{turb}}| = 0.1$. This suggests a flow regime change at $|\lambda_{\text{turb}}| \approx 0.1$, beyond which the throughflow dominates over rotation. This gives further evidence to $|\lambda_{\text{turb}}| \approx 0.1$ being the demarcation point for the two flow regimes. For the swirl level plateau hypothesis to be valid, conversely, the profile of $V_z / \Omega r$ should register a steep increase for $|\lambda_{\text{turb}}| > 0.1$, (after transition to a throughflow-dominated regime); this is shown in Fig. 8 (b). As expected, the rotor and stator boundary-layer thickness grow with increasing $|C_w|$, and for $|C_w| \geq 42000$, i.e. $|\lambda_{\text{turb}}| \geq 0.4$, the central core ceases to exist, when the two boundary-layers merge.

Fig. 9 (a) shows the predicted radial distribution of $V_\phi / \Omega r$ at the plane $y = 0.65$, for the downstream cavity. Interestingly, for $|\lambda_{\text{turb}}| \geq 0.1$, the swirl ratio near the rotor appears to be “limited” to 0.65, until a further increase of up to $|\lambda_{\text{turb}}| = 0.8$ causes the level of swirl to rise further towards rotor speed. This is due to a slight change in flow regime near the drive cone inner radii (see Fig. 6); for $|\lambda_{\text{turb}}| \leq 0.4$, there still exists a small recirculation near the cone inner radii, and when $|\lambda_{\text{turb}}| = 0.8$, that recirculation is fully suppressed, and the flow travels axially along the rotor surface before moving radially outwards towards the exit. Examination of the local value of $V_\phi / \Omega r$ in Fig. 9 (a) reveals a value of 0.8, for $|\lambda_{\text{turb}}| = 0.8$. From just the radial momentum point of view, the radial pressure gradient due to the rotation at $V_\phi / \Omega r = 0.8$ is still insufficient to overcome the centrifugal pumping; however, the flow also carries a significant amount of axial momentum, hence the radial inflow along the rotor surface for $|\lambda_{\text{turb}}| = 0.8$. This slight change of flow regime is also reflected in the computed axial velocity distribution in Fig. 9 (b), where there is a sudden reversal of flow direction for $|\lambda_{\text{turb}}| = 0.8$.

6. CONCLUSIONS

Overall, the agreement between the measured and predicted tangential and axial velocities in both the upstream and downstream cavities using an axisymmetric model is satisfactory. Qualitative (but not quantitative) agreement was observed, where the measured Rankine vortex profiles was computed by CFD: the effect of $|C_w|$ on radial distributions of $V_\phi / \Omega r$ was predicted satisfactorily; but, core rotation tends to be underestimated by CFD, although agreement improves with decreasing $|C_w|$ i.e. decreasing $|\lambda_{\text{turb}}|$. For all cases with no throughflow, CFD consistently predicted the theoretical value $\beta^* = 0.426$. The computed streamlines for $|\lambda_{\text{turb}}| \leq 0.8$ show that the cone cavity flow structure depend principally on $|\lambda_{\text{turb}}|$, for inlet swirl between 0.3 and 0.5.

Examination of the velocity profiles at the upstream and downstream planes ($y = 0.36$ and 0.65 , respectively) and the streamlines from CFD suggested two flow regimes. For computations of $0.2 \leq \text{Re}_\phi / 10^7 \leq 2$, $0 \leq |C_w| / 10^5 \leq 1.7$, $0 \leq |\lambda_{\text{turb}}| \leq 0.8$, and $0.3 \leq c \leq 0.5$: $|\lambda_{\text{turb}}| \approx 0.1$ was postulated as the demarcation point between a rotationally- and a throughflow-dominated regime, existing for $0 \leq |\lambda_{\text{turb}}| < 0.1$ and $|\lambda_{\text{turb}}| > 0.1$, respectively. This gains further support from the analysis of the cone moment coefficients from CFD, which will be presented in a future paper.

ACKNOWLEDGMENTS

The authors would like to thank the following organisations: The Engineering and Physical Sciences Research Council; Rolls-Royce plc; the European Union and participating companies in the 4th Framework of the BRITE-EURAM scheme of the European Union. We are also grateful to Dr. A. Alexiou for the LDA measurements.

REFERENCES

British Standards Institute (1992), “BS1042: Measurement of Fluid

Flow in Closed Conduits, Section 1.1: Specification for Square-Edged Orifice Plates, Nozzles, and Venturi Tubes Inserted in Circular Cross-Section Conduits Running Full.”

Chew, J.W. (1985), “Moment Coefficients and Flow Entrainment Rate for a Cone Rotating in an Infinite Environment,” Rolls-Royce Internal Report No. TSG0225.

FLUENT (1998), “Fluent 5 User’s Guide,” Fluent Inc, Lebanon, NH.

GAMBIT (1998), “Gambit User’s Guide,” Fluent Inc, Lebanon, NH.

Gan, X., Mirzaee, I., Owen, J.M., Rees, D.A.S. and Wilson, M. (1996), “Flow in a Rotating Cavity with a Peripheral Inlet and Outlet of Cooling Air,” ASME Paper No. 96-GT-309.

Jaafar, A.A., Motallebi, F., Wilson, M. and Owen, J.M. (2000), “Flow and Heat Transfer in a Rotating Cavity With a Stationary Stepped Casing,” ASME Paper No. 2000-GT-281.

Ko, S.H. and Rhode, D.L. (1992), “Thermal Details in a Rotor-Stator Cavity at Engine Conditions with a Mainstream,” *ASME Journal of Turbomachinery*, Vol. 114, pp. 446-453.

Lauder, B.E. and Spalding, D.B. (1972), “Lectures in Mathematical Models of Turbulence,” Academic Press, London, England.

Long, C.A., Turner, A.B., Kais, G., Tham, K.M., and Verdicchio, J.A. (2003), “Measurement and CFD Prediction of the Flow Within an H.P. Compressor Drive Cone,” *ASME Journal of Turbomachinery*, Vol. 125, pp. 165-172.

May, N.E., Chew, J.W. and James, P.W. (1994), “Calculation of Turbulent Flow for an Enclosed Rotating Cone,” *ASME Journal of Turbomachinery*, Vol. 116, pp. 548-554.

Mirzaee, I., Gan, X., Wilson, M. and Owen, J.M. (1998), “Heat Transfer in a Rotating Cavity With a Peripheral Inflow and Outflow of Cooling Air,” *ASME Journal of Turbomachinery*, Vol. 120, pp. 818-823.

Owen, J.M. (1988), “An Approximate Solution for the Flow Between A Rotating and A Stationary Disc,” *ASME Journal of Turbomachinery*, Vol. 111, pp. 323-332.

Patankar, S.V. and Spalding, D.B. (1972), “A Calculation Procedure for Heat, Mass and Momentum Transfer in Three-Dimensional Parabolic Flows,” *International Journal of Heat and Mass Transfer*, Vol. 15, pp. 1787-1806.

Taylor, G.I. (1923), “Stability of a Viscous Liquid Contained between Two Rotating Cylinders,” *Philosophical Transactions of the Royal Society*, Series A, Vol. 223, pp. 289-343.

Turner, A.B., Davies, S.J., Childs, P.R.N., Harvey, C.G. and Millward, J.A. (2000), “Development of a Novel Gas Turbine Driven Centrifugal Compressor,” *Proceedings of the Institution of Mechanical Engineers*, Part A, Vol. 214, pp. 423-437.

Wu, C.-S. (1959), “The Three Dimensional Incompressible Laminar Boundary Layer on a Spinning Cone,” *Applied Scientific Research*, Sec. A, Vol. 8, pp. 140-146.

Yamada, Y. and Ito, M. (1979), “Frictional Resistance of Enclosed Rotating Cones With Superposed Throughflow,” *ASME Journal of Fluids Engineering*, Vol. 101, pp. 259-264.